Appendix B

Protein-Signaling Networks from Single-cell Fluctuations and Information Theory Profiling

B.1. Introduction

Protein-signaling pathways play important roles in tissue processes ranging from tumorigenesis to wound healing[1-5]. Elucidation of these signaling pathways is challenging, in large part, because of the heterogeneous nature of tissues[6]. Such heterogeneity makes it difficult to separate cell-autonomous alterations in function from alterations that are triggered via paracrine signaling, and it can mask the cellular origins of paracrine signaling. Intracellular signaling pathways can be resolved via multiplex protein measurements at the single-cell level[7]. For secreted protein signaling, there are additional experimental challenges. Intracellular staining flow cytometry (ICS-FC) requires the use of protein transport inhibitors which can influence the measurements[8]. In addition, the largest number of cytokines simultaneously assayed in single-cells by ICS-FC is only 5[9]. Finally, certain biological perturbations, such as the influence of one cell on another, are difficult to decipher using ICS-FC. Other methods, such as multiplex fluorospot assays[10], have even more significant limitations.

We describe here an experimental/theoretical approach designed to unravel the coordinated relationships between secreted proteins, and to understand how molecular and cellular perturbations can influence those relationships. Our starting points are single, lipopolysaccharide (LPS)-stimulated, human macrophage cells[11]. LPS stimulation activates the Toll-like Receptor-4 (TLR-4), and emulates the innate immune response to Gram-negative bacteria. We characterize the secretome, at the single-cell level, through the use of a microchip platform in which single, stimulated macrophage cells are isolated into 3 nanoliter (nl) volume microchambers, with ~1000 microchambers per chip. Each microchamber permits duplicate assays for each of a dozen proteins that are secreted over the course of a several-hour incubation period following cell stimulation. The barcode assays are developed using detection antibodies and fluorescent labels, and then converted into numbers of molecules detected. We demonstrate that the observed spread in protein

levels is dominated by the cellular behaviors (the biological fluctuations), rather than the experimental error. These fluctuations are utilized to compute a covariance matrix linking the different proteins. This matrix is analyzed at both coarse and fine levels to extract the protein-protein interactions. We demonstrate that our system has the stability properties requisite for the application of a quantitative version of a Le Chatelier-like principle, which permits a description of the response of the system to a perturbation. This is a prediction in the strict thermodynamic sense. The fluctuations, as assessed from the multiplexed protein assays from unperturbed single-cells, are used to predict the results when the cells are perturbed by the presence of other cells, or through molecular (antibody) perturbations.

B.2. EXPERIMENTAL METHODS

B.2.1. Microchip fabrication.

The SCBCs were assembled from a DNA barcode microarray glass slide and a PDMS slab containing a microfluidic circuit[12,13]. The DNA barcode array was created with microchannel-guided flow patterning technique[13]. Each barcode was comprised of thirteen stripes of uniquely designed ssDNA molecules. PDMS microfluidic chip was fabricated using a two-layer soft lithography approach[14]. The control layer was molded from a SU8 2010 negative photoresist (~20 μm in thickness) silicon master using a mixture of GE RTV 615 PDMS prepolymer part A and part B (5:1). The flow layer was fabricated by spin-casting the pre-polymer of GE RTV 615 PDMS part A and part B (20:1) onto a SPR 220 positive photoresist master at ~2000 rpm for 1minute. The SPR 220 mold was ~18 mm in height after rounding via thermal treatment. The control layer PDMS chip was then carefully aligned and placed onto the flow layer, which was still situated on its silicon master mold, and an additional 60 min thermal treatment at 80 °C was performed to enable bonding. Afterward, this two-layer PDMS chip was cut off and access holes drilled. In order to improve the biocompatibility of PDMS, we performed a solvent extraction step, which removes uncrosslinked oligomers, solvent and residues of the curing agent through serial extractions/washes of PDMS with several solvents[15,16]. We noticed that this step significantly improves the biocompatibility and the reproducible protein detection. Finally, the microfluidic-containing PDMS slab was thermally bonded onto the barcode-patterned glass slide to give a fully assembled microchip.

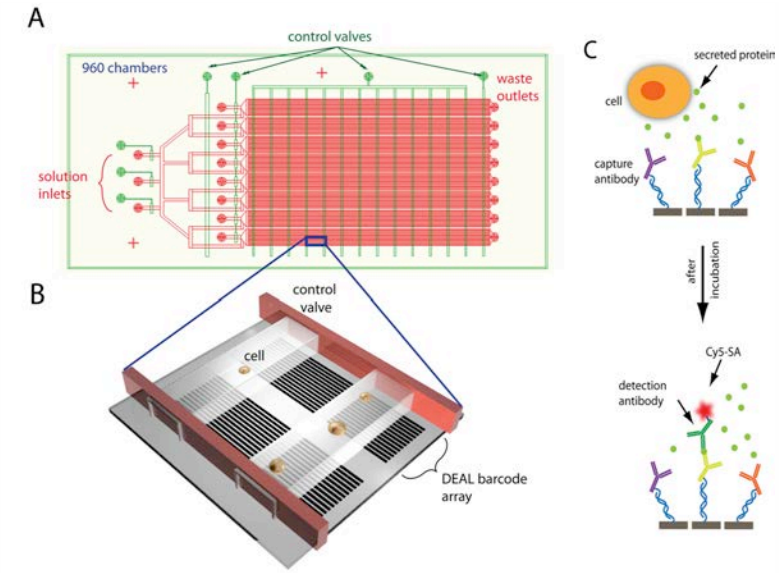

Fig. B.1. Design of integrated microchip for single-cell protein secretome analysis. (A) CAD design of a microchip in which flow channels are shown in red and the control channels are shown in green. (B) Schematic drawing of cells loaded in the microchambers and compartmentalized with the valves pressurized. (C) Schematic illustration of the antibody barcode array used for multiplexed immunoassay of single-cell secreted proteins.

B.2.2. Preparation of barcode arrays

The barcode array initially consists of 13 uniquely designed DNA strands labeled in order as A through M. Prior to loading cells, a cocktail containing all capture antibodies conjugated to different complementary DNA strands (A'-L') is flowed through the chambers, thus transforming, via DNA-hybridization, the DNA barcode into an antibody array. These dozen proteins that comprised the panel used here were encoded by the DNA strands A through L, respectively. Calibration and cross-reactivity curves for each protein assay are in **Fig. B.2.**, The DNA oligomer sequences and the antibody pairs used are listed in **Table B.1.** and **Table B.2.**

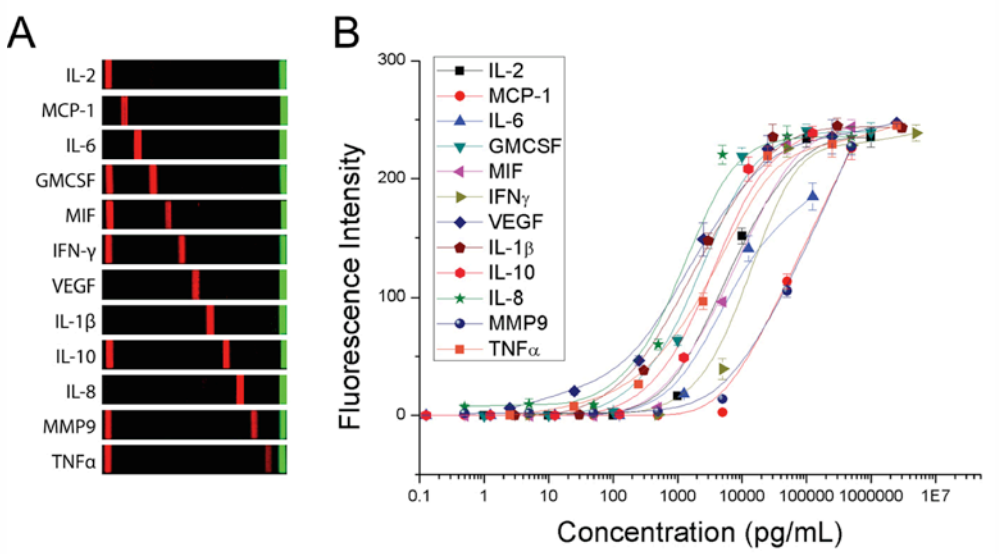

Fig. B.2. Cross-reactivity check and calibration curves. (A) Scanned image showing cross-reactivity check for all 12 proteins. The green bars represent the reference stripe, sequence M. Each protein can be readily identified by its distance from the reference. In each channel, a standard protein (indicated on the left) was added to the buffer solution and assayed using the DEAL barcode method. For GMCSF, MIF, IFN-γ, IL-10, MMP9, and TNF-α, biotin-labeled 2° anti IL-2 antibody conjugated to DNA sequence A' was used as a control. (B) Quantitation of fluorescence intensity vs. concentration for all 12 proteins. Error bars: 1SD. The variability (defined as the standard deviation divided by the average in percentage) is less than 10% for the signals in detectable range.

Table B.1. Sequences and terminal functionalization of oligonucleotides*.

Name	Sequence
A	5'- AAA AAA AAA AAA AGT CCT CGC TTC GTC TAT GAG-3'
A'	5' NH3-AAA AAA AAA ACT CAT AGA CGA AGC GAG GAC-3'
B	5'-AAA AAA AAA AAA AGC CTC ATT GAA TCA TGC CTA -3'
B'	5' NH3-AAA AAA AAA ATA GGC ATG ATT CAA TGA GGC -3'
C	5'- AAA AAA AAA AAA AGC ACT CGT CTA CTA TCG CTA -3'
C'	5' NH3-AAA AAA AAA ATA GCG ATA GTA GAC GAG TGC -3'
D	5'-AAA AAA AAA AAA AAT GGT CGA GAT GTC AGA GTA -3'
D'	5' NH3-AAA AAA AAA ATA CTC TGA CAT CTC GAC CAT -3'
E	5'-AAA AAA AAA AAA AAT GTG AAG TGG CAG TAT CTA -3'
E'	5' NH3-AAA AAA AAA ATA GAT ACT GCC ACT TCA CAT -3'
F	5'-AAA AAA AAA AAA AAT CAG GTA AGG TTC ACG GTA -3'
F'	5' NH3-AAA AAA AAA ATA CCG TGA ACC TTA CCT GAT -3'
G	5'-AAA AAA AAA AGA GTA GCC TTC CCG AGC ATT-3'
G'	5' NH3-AAA AAA AAA AAA TGC TCG GGA AGG CTA CTC-3'
H	5'-AAA AAA AAA AAT TGA CCA AAC TGC GGT GCG-3'
H'	5' NH3-AAA AAA AAA ACG CAC CGC AGT TTG GTC AAT-3'
I	5'-AAA AAA AAA ATG CCC TAT TGT TGC GTC GGA-3'
I'	5' NH3-AAA AAA AAA ATC CGA CGC AAC AAT AGG GCA-3'
J	5'-AAA AAA AAA ATC TTC TAG TTG TCG AGC AGG-3'
J'	5' NH3-AAA AAA AAA ACC TGC TCG ACA ACT AGA AGA-3'
K	5'-AAA AAA AAA ATA ATC TAA TTC TGG TCG CGG-3'
K'	5' NH3-AAA AAA AAA ACC GCG ACC AGA ATT AGA TTA-3'
L	5'-AAA AAA AAA AGT GAT TAA GTC TGC TTC GGC-3'
L'	5' NH3-AAA AAA AAA AGC CGA AGC AGA CTT AAT CAC-3'
M	5'-AAA AAA AAA AGT CGA GGA TTC TGA ACC TGT-3'
M'	5' Cy3-AAA AAA AAA AAC AGG TTC AGA ATC CTC GAC-3'

* All oligonucleotides were synthesized by Integrated DNA Technology (IDT) and purified via high-performance liquid chromatography (HPLC).

Table B.2. Summary of antibodies used for macrophage experiments

DNA label	primary antibody (vendor)	secondary antibody (vendor)
A'	mouse anti-hu IL-2 (BD Biosciences)	biotin-labeled mouse anti-hu IL-2 (BD Biosciences)
B'	mouse anti-hu MCP-1 (eBioscience)	biotin-labeled armenian hamster anti-hu MCP-1 (eBioscience)
C'	rat anti-hu IL-6 (eBioscience)	biotin-labeled rat anti-hu IL-6 (eBioscience)
D'	rat anti-hu GMCSF (Biolegend)	biotin-labeled rat anti-hu GMCSF (Biolegend)
E'	goat anti-hu MIF(R&D systems)	biotin-labeled goat anti-hu MIF(R&D systems)
F'	mouse anti-hu IFN-□ (eBioscience)	biotin-labeled mouse anti-hu IFN-□ (eBioscience)
G'	mouse anti-hu VEGF (R&D systems)	biotin-labeled goat anti-hu VEGF (R&D systems)
H'	mouse anti-hu IL-1β (eBioscience)	biotin-labeled mouse anti-hu IL-1β (eBioscience)
I'	rat anti-hu IL-10 (eBioscience)	biotin-labeled rat anti-hu IL-10 (eBioscience)
J'	mouse anti-hu IL-8 (R&D systems)	biotin-labeled mouse anti-hu IL-8 (R&D systems)
K'	mouse anti-hu MMP9 (R&D systems)	biotin-labeled goat anti-hu MMP9 (R&D systems)
L'	mouse anti-hu TNF-α (eBioscience)	biotin-labeled mouse anti-hu TNF-α (eBioscience)

B.2.3. Culture and stimulation of THP-1 cells.

We cultured human monocyte THP-1 cells (clone TIB 202) in RPMI-1640 (ATCC) medium supplemented with 10% fetal bovine serum and 10 μM 2-mercaptoethanol. Cells grown close to the maximum density (0.8×10^6 cells/mL) were chosen for the experiment. Cells were first treated with 100 ng/mL phorbol 12-myristate 13-acetate (PMA) for 12 hours during which a characteristic morphological change was noticed as an indication of the induction to the macrophages. Cells were washed with fresh media and re-suspended in media with PMA (100 ng/mL) and lipopolysaccharide (LPS, 200 ng/mL) at 0.5×10^6 cells/mL for the further differentiation and the TLR-4 activation.

B.2.4. On-chip secretion profiling

Prior to loading cells on chip, the DNA barcode array was transformed into an antibody microarray through the following steps. First, 1% bovine serum albumin (BSA) in phosphate buffered saline (PBS) was flowed and dead-end filled into the chip to block non-specific binding. Second, a 200 ml cocktail containing all 12 DNA-antibody conjugates at 1.25 μg/mL in 1% BSA/PBS buffer was flowed through all microfluidic channels for a period of 1 h. Then, 100 ml of fresh buffer was flowed into the device to replace DNA conjugated primary antibody solutions. The chip is then ready for use. Cells stimulated

with PMA/LPS were loaded into the SCBC chip within 10 min in order to minimize pre-loading secretion. Then, the pneumatic valves were pressed down by applying 15-20 psi constant pressure to divide 80 microfluidic channels into 960 isolated microchambers. Next, the cells in every microchamber were imaged under a Nikon LV100 microscope and their numbers were counted. Afterwards the chip was placed in a cell incubator (~37 $^{\circ}$C and 5% CO_2) for 24 hours to perform on chip secretion. The chip was removed from the incubator and a 200 ml cocktail containing all detection antibodies (each at 0.5 μg/mL concentration) tagged with biotin flowed through the microchannels by releasing the valves. Then, 200 μl of the fluorescent probe solution (1 μg/ml Cy5-labeled streptavidin and 25 nM Cy3-labeled M' ssDNA) was flowed through to complete the immuno-sandwich assay. Finally, the PDMS slab was peeled off and the microarray slide was rinsed with 1×PBS, 0.5×PBS and DI water twice, sequentially, and spin-dried.

B.2.5. Bulk secretion profiling

Bulk measurements on the same panel of secreted proteins as were assessed within the SCBC microchambers were also carried out for the THP-1 cells with no stimulation, PMA stimulation, and PMA+LPS stimulation. Cells were cultured at 0.3×10^6 cells/mL, a comparable density to a single-cell in a chamber. The media were collected after 24 hours and the secreted proteins were detected as described below. For the PMA+LPS stimulation condition, the media were collected at multiple time points (2, 4, 6, 8, and 10 hours) for the time-dependent analysis as well. For the bulk test, SCBC chip was utilized without using valves for the microchannel to microchamber conversion. The same conditions as for the on-chip secretion profiling were applied except for the cell incubation step. Instead, the collected media was introduced to the channel sets and incubated for 3 hours in the incubator.

B.2.6. Quantification and statistics.

All the barcode array slides used for quantification were scanned using an Axon GenePix 4400a two-color laser microarray scanner at the same instrumental settings—50% and 15%

for the laser power of 635 nm and 532 nm, respectively. Optical gains are 500 and 450 for 635 nm and 532 nm fluorescence signals, respectively. The brightness and contrast were set at 90 and 93. The averaged fluorescence intensities for all barcodes in each chamber were obtained and matched to the cell number by custom-developed MATLAB (the mathworks, Natick, MA) codes. Heat maps were generated using cluster 3.0 and java *treeview* (http://rana.lbl.gov/eisensoftware.htm).

B.2.7. Data Analysis: Conversion to the number of molecules

The collected raw data is based on the fluorescence. In order to convert the fluorescence to the number of protein molecules, we used the calibration curves (**Fig. 3.2.**). We used the four parameter logistic model which is commonly used for fitting ELISA calibration curve. The fitting parameters can be found from the **Table 3.3.**

$$y = \frac{A_1 - A_2}{1 + (x / x_0)^p} + A_2$$

Table 3.3. Parameters utilized for the protein assay calibration curve

	A1		A2		x0		p		Statistics	
	Value	Error	Value	Error	Value	Error	Value	Error	Reduced Chi-Sqr	Adj. R-Square
IL-2	0	0	256	0	7659.58168	973.0838	1.12824	0.16788	91.39131	0.99224
MCP-1	0	0	256	0	65733.51686	4770.5	1.12607	0.09607	29.62623	0.99578
IL-6	0	0	256	0	16231.59942	4515.94	0.67887	0.12265	243.09932	0.95697
GMCSF	0	0	256	0	2451.99685	295.3281	1.2195	0.13013	72.59138	0.99458
MIF	0	0	256	0	7892.74068	483.8218	1.14428	0.07578	20.31714	0.99821
IFN-γ	0	0	256	0	14549.5316	2773.804	1.57222	0.26181	172.2368	0.98713
VEGF	0	0	256	0	1687.9445	225.4782	0.69008	0.05631	58.49911	0.99513
IL-1β	0	0	256	0	2137.44388	208.9672	0.89593	0.07185	41.21361	0.99694
IL-10	0	0	256	0	3961.03661	328.4038	1.23209	0.08611	33.93572	0.99669
IL-8	0	0	256	0	1255.89317	225.9207	1.23262	0.19534	161.8703	0.98686
MMP9	0	0	256	0	70537.40022	1584.696	1.062	0.02495	2.60945	0.99961
TNF-α	0	0	256	0	4126.15703	661.2747	0.81683	0.09483	99.72583	0.99185

B.2.8. Signal-to-noise calculations

Since the signal range highly depends on the activities of the antibodies as well as the cell biology, it is required to decide if the signal is real and reliable. Certain assayed

proteins were identified as positively detected from single-cells based upon signal-to-noise ratio (S/N), which was measured as follows: For each microchamber, the averaged fluorescence from the two barcode stripes used to capture and detect a given protein and the averaged fluorescence from the barcode stripes designed to capture and detect IL-2 were obtained. The ratio of the averaged values over all single-cell experiments (specific protein to IL-2) yields a S/N value. An S/N of 4 was utilized as a minimum for positive detection. Eight secreted proteins were thus identified from the single-cell measurements. Those proteins were (with S/N included in the parenthesis after the protein name): MCP-1 (4.65), MIF (1381.13), IFN-γ (4.33), VEGF (77.32), IL-1β (94.70), IL-8 (2622.40), MMP9 (119.50), and TNF-α (410.74).

B.2.9 Analysis of experimental and biological variation from SCBC-based single-cell measurement

One of the major characteristics of SCBC analysis is the heterogeneous cellular behavior at single-cell level. The experimental variation of the SCBC platform which reflects the system error as well as the biological variation due to the cellular heterogeneity is contributing to the fluctuation of the total signal. Thus, we need to check if the heterogeneous signal responses are from the cells or the device itself.

The experimental error mainly includes the variation from non-uniform DNA barcode patterns and the variation due to the randomly distributed cell location in the chamber. The former one can be estimated by the histogram of the fluorescence intensity from the calibration experiment with recombinant proteins. Since the recombinant protein has fixed concentration over the entire channel, it represents a uniform protein level without any heterogeneity and location dependence. As a result, the distribution of the fluorescence intensity of a specific recombinant reflects the detection profile of the DNA barcode.

Fig. B.3.A shows a representative histogram of signal derived from recombinant MIF protein at 5 ng/ml. The histogram shows a nice Gaussian distribution with a coefficient of variation (CV) around 7%. In the calibration experiment, basically the intensities of all the recombinant proteins at detectable concentrations follow a Gaussian distribution with CVs typically lower than 10%.

The cell location is another important factor for the system error. Even though the chamber size is small, it is still big for a single-cell. So the protein signal is dependent on diffusion and that is why the cell location can be a source of the variation. In order to minimize this effect, we utilized two sets of barcodes in a chamber and used the averaged signal intensity from two barcodes as the final signal value. However, the barcode close to the cell will undergo a higher local protein concentration than its counterpart and the different intensities of two sets of barcodes are amplified during the long incubation time. The diffusion process will lead the system close to the equilibrium but the cell that keeps secreting proteins with different kinetics makes it difficult for the chamber to reach its full equilibrium. In that sense, the randomly located cells can add an extra uncertainty to the SCBC system.

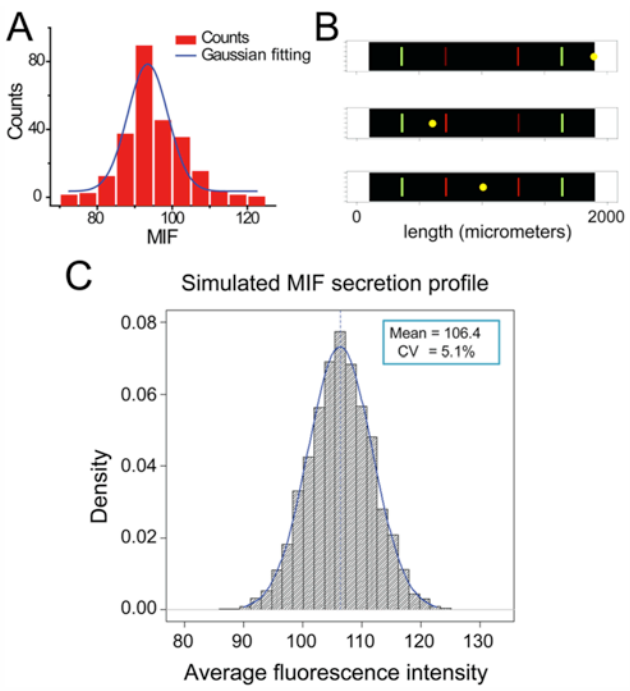

Fig. B.3. Experimental and simulation results for extracting the experimental error contribution to the SCBC protein assays. (A) Representative histogram of signal measured from individual barcode stripes for assaying a 5 ng/ml solution of recombinant MIF protein, representing a Gaussian distribution with a coefficient of variation (CV) near 7%. (B) Monte Carlo simulated barcode intensity (corresponding to MIF) versus cell location in three single-cell chambers. Yellow dots represent cell locations, and the brightness of the red stripes reflects the simulated signal level. The cell-location effect is minimized by averaging the signals from both barcodes. (C) Histogram from simulations of 5000 single-cell experiments. For this simulation, the diffusion equation was solved with a randomly located, continuously secreting cell. The histogram represents the averaged intensities over both barcodes, and includes the experimentally determined barcode variability.

Because it is difficult to isolate the system error (especially for the cell-location effect) from the heterogeneous cell response experimentally, we performed a Monte Carlo simulation by R (R Foundation for Statistical Computing, version 2.10.1). First of all, we investigate the case of MIF as a representative case. We assumed one chamber has

two sets of 13 barcodes such that all of them have MIF antibodies. By randomly positioning a cell with a fixed protein secretion rate and getting the protein concentration at specific barcode positions, we can find out what is the variation that purely depends on the cell location and barcode non-uniformity. The total amount of secreted MIF during 24 hours was estimated based on our experimental result. The secretion rate was 4.84 pg/mL per min from the SCBC (used for the simulation) and 11 pg/mL per min from the bulk condition. The corresponding secretion rate of a single-cell, back-calculated based on the chamber and cell size ($10\mu m^3$), was 0.065 nM/min. Values of parameters used in simulation can be found from **Table B.4.** 5000 data sets for the protein concentration distributions from randomly located single-cell were generated by solving a diffusion equation with a custom made MATLAB code and the results were analyzed with R. The parameters used in the simulation are exactly the same as our experimental environment. The chamber is 2000 μm in length and 100 μm in width with two sets of DNA barcodes M-A and A-M from left to right. Each barcode is 20 μm in width with 50 μm in pitch (30μm gap between barcodes). The detection variation of the MIF protein due to the DNA uniformity obtained from the histogram of the calibration data set was incorporated to the analysis. **Fig. B.3.C** shows the histogram of the average fluorescence intensity from DNA sequence E (corresponding to MIF in the actual experiment) for 5000 single-cell cases. For the barcode variability, the actual value of 7.3% was used. The final system error was 5.1% which is a lot smaller than the assay error from the experimental data sets, 55.2 %.

Table B.4. Values of parameters used in simulation

Chamber size	2000 μm×100 μm ×18 μm
Cell diameter	10 μm
Diffusion Coefficient(11)	10^{-6} cm^2/sec
Protein secretion rate (MIF)	0.065 nM/min
Molecular weight	12500 Da

In order to think of the worst case, we used the barcode variability of 10% for the rest of the analysis. If the cell-location effect is significant, we are supposed to see different

errors on different barcode positions. **Fig. B.4.** illustrate the histograms of average intensities from multiple barcode locations. The blue curves are line profiles of Gaussian distribution fitted with the mean and the standard deviation obtained from the corresponding simulation. The nice fitting between the Gaussian curves and the histogram indicates that the average intensity per chamber follows a Gaussian distribution with a predictable mean and CV. The CVs from this simulation represent the distribution of our measurements for single-cell chambers without considering the cellular heterogeneity, i.e. the system error. The experimental CVs for different barcode locations based on the system error were quite similar to one another (~ 7%).

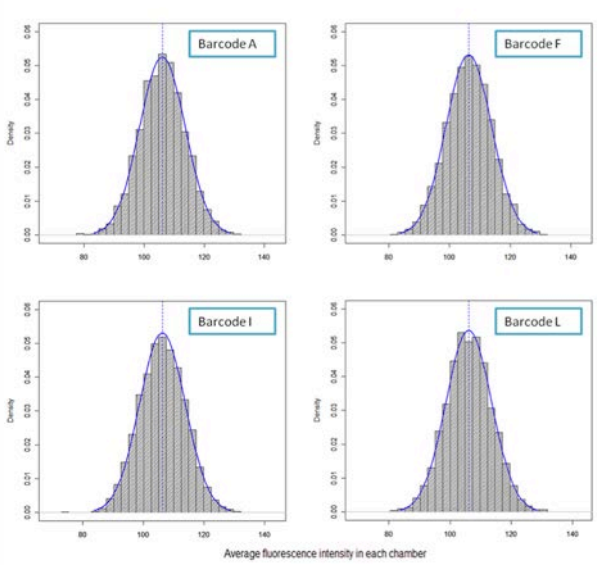

Fig. B.4. Simulated histograms of average intensity from multiple DNA barcode locations. The signal intensities for 5000 single-cell data sets were obtained by solving a diffusion equation for a randomly located cell. For the barcode variability, the value of 10% was used. The blue curves are the Gaussian fitting of the histogram with sample mean and sample standard deviation from the simulation.

We can define CV_{system} as the system error estimated by the simulation. We can also calculate the assay error from our experimental data set such that CV_{assay} refers to the total CV of our experimental data. Consequently, the biological variation for single-cell experiment can be quantitatively estimated by the formula below:

$$CV_{assay} = (CV^2_{system} + CV^2_{biological})^{1/2}$$

An estimation of biological variations of proteins for different barcode locations are shown in **Table B.5.** It can be noticed that the biological variation is dominant in the total error of the assay. This analysis verifies that the signal fluctuation that we can see from the single-cell experiment is a good representation for the single-cell heterogeneity rather than the systemic error from our platform.

Table B.5. The coefficients of variation for each of the assayed proteins from single-cell experiments. The experimental CVs are estimated from the Monte Carlo simulations. The biological CVs, which clearly dominate the experiment, are calculated from $CV_{\text{assay}} = (CV^2{}_{\text{system}} + CV^2{}_{\text{biological}})^{1/2}$.

Barcode/Protein	Experimental CV (%)	Assay CV (%)	Biological CV (%)
B / MCP-1	7.12	380.4	380.3
E / MIF	7.05	55.2	54.7
F / IFN-γ	7.04	131.5	131.3
G / VEGF	7.03	149.7	149.5
H / IL-1β	7.02	300.6	300.5
J / IL-8	7.00	14.4	12.6
K / MMP9	6.98	192.6	192.5
L / TNF-α	6.97	132.9	132.7

B.2.10 Signal-to-noise calculations and experimental error

An Axon GenePix 4400A scanner coupled with a custom algorithm was used to quantify the fluorescence intensities of each protein from each microchamber (Fig 1B). Certain proteins were positively detected based upon signal-to-noise (S/N) > 4. S/N was calculated as follows. Each protein was measured twice per microchamber. The averaged fluorescence values from the two barcode stripes for all proteins were used as signals from each chamber. The ratio of the averaged signal over all single-cell experiments for a specific protein to IL-2 yields a S/N. The following eight proteins were detected (S/N is indicated after the protein name): MCP-1 (4.7), MIF (1380), IFN-g (4.3), VEGF (77), IL-1b (95), IL-8 (2620), MMP9 (120), and TNF-a (411).

Macrophages are highly responsive to their environment, and so experimental conditions can influence macrophage behavior. Thus, we sought confirmation that our protocols could lead to reproducible results. We executed identical sets of experiments on different SCBCs, and showed that the distributions of the unambiguously detected proteins

were effectively identical (p-value > 0.25). The results presented here do depend on the amount of PMA or LPS used and, to a lesser extent, the passage number of THP-1 cells. In addition, a solvent extraction of the PDMS improves the SCBC biocompatibility and the assay reproducibility[15].

Levels of proteins secreted from single-cells can exhibit a variability that reflects the stochastic nature of biology[17] and, in fact, represents the biological fluctuations. The SCBC experimental error must be compared against the measured variations for extracting the true macrophage fluctuations. One contribution to the experimental error arises from the variability of the flow-patterned antibody barcodes. We characterized that variability via protein assays executed within a complex biological environment (serum), and within the microchambers of an SCBC, but using cocktails spiked with known quantities of standard proteins. In both cases, we found a variability of < 10%[18] and **Fig. B.2.**), depending upon the protein. Averaging the two identical protein assays per microchamber lowers the variability within a microchamber by a factor of $2^{½}$. A second experimental error arises from the competition between protein capture by surface-bound antibody, and protein diffusion. When a cell is proximal to a barcode, that barcode may exhibit a higher signal intensity than the more distant barcode. A Monte Carlo calculation allowed for an estimation of the total system error by simulating the location-dependent experimental variation. Using MIF as a representative protein for the simulation (it has a barcode variability of 7.3%; **Fig. B.3.A**) the experimental error of the system is estimated to be 5.1% (**Fig. B.3.B, C**). For the worst case of a 10% barcode variability, the total experimental error is estimated to be ~7% (**Table B.5.** and **Fig. B.4.**). Based upon these results, we can calculate the biological coefficient of variation ($CV_{\text{biological}}$) from $CV_{\text{assay}} = (CV^2{}_{\text{system}} + CV^2{}_{\text{biological}})^{1/2}$, where CV_{assay} is the measured spread in secretion levels for a given protein across all measurements for a given number of cells. For IL-8, the biological CV was only ~2-fold larger than the experimental CV, but for the other 7 detected proteins, the biological CV was 7-50× larger than the experimental CV (**Table B.5.**). Thus, the fluctuation extracted from our single-cell experiments reflects the cellular behaviors.

The individual protein assays were evaluated for cross-reactivity and calibrated using standard proteins (**Fig. B.2.**). Calibration curves were fitted by a four parameter logistic

model[19]. The SCBC assay sensitivities are comparable to commercial ELISAs (e.g., a few measured limits-of-detection are MIF ~100 pg/ml, IL-8 ~50 pg/ml, IL-1b~20 pg/ml, and VEGF ~2.5 pg/ml), with each exhibiting a ~10^3 linear detection range. The SCBC barcode assay results can be translated into numbers of detected molecules using the molecular weight of the standard proteins and the microchamber volume (**Fig. B.2.**). This quantitative representation of the data is used for the calculations described below. However, the standard proteins may differ from the proteins secreted by the macrophages (for example, glycosylation patterns may vary). Such variations can translate into differences in molecular weight, as well as differences in assay sensitivity.

The experimental results, presented as the number of cells per experiment, are shown in the heat maps of **Fig. B.5.**

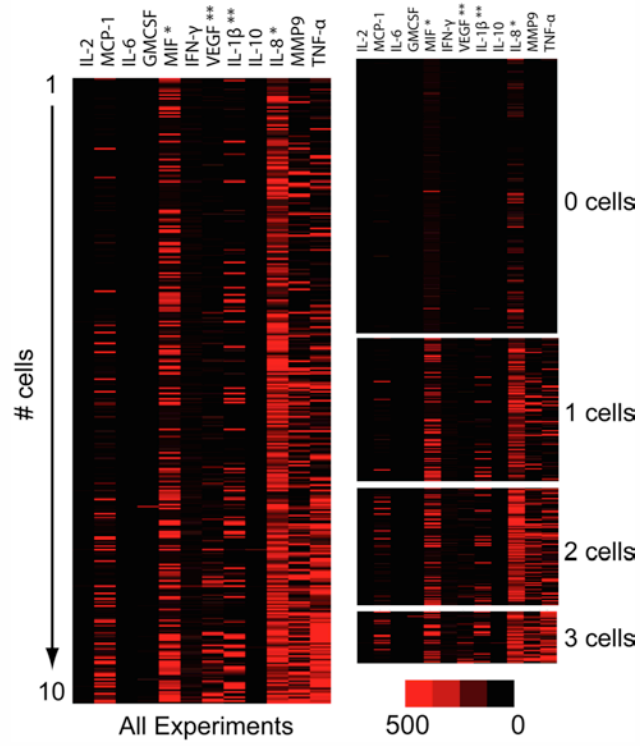

Fig. B.5. Protein secretion heat maps for different colony sizes of LPS-stimulated macrophages. Each row represents one microchamber assay, and each column represents protein level, as measured in copy numbers of each protein. The zero cell heat map is the background signal. Signals are decreased and amplified 10× for * and **, respectively.

B.3. THEORETICAL METHODS

B.3.1. The fluctuations in the secretome

The calibrated experimental data can be organized into digital tables of twelve columns, each representing a different protein, with different tables representing different numbers of cells in the microchamber. For a given table, each row represents the copy numbers of the twelve proteins for a single-cell, or small cell colony. For a given table, if the number of measurements is large enough, we can bin the data for each individual protein into a histogram with each bin representing a defined range of measured levels (**Fig. B.6.**). With even more measurements one could generate joint distributions between two proteins, etc. However, we first confine our attention to the individual protein histograms because they provide a natural meeting place for experiment and theory. The theoretical prediction is made by seeking that distribution of copy numbers that is of maximal entropy, meaning that the distribution is as uniform as possible subject to a given mean number of copies[20-23]. As described in detail in the Supplement, We use the distribution of maximal physical entropy. This means that at the very global maximum of the entropy, the probabilities of the different proteins are not equal. Rather, as in any multi-component system at thermal equilibrium, each protein will be present in proportion to its partition function [24] where the partition function is the effective thermodynamic weight of a species at thermal equilibrium. We show below that in our system there is a network structure that imposes (at least) two overriding constraints that preclude the system from being in thermal equilibrium.

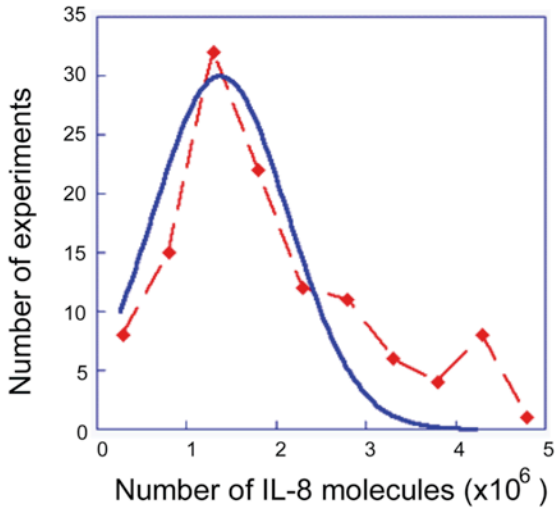

Fig. B.6. Fluctuations in the numbers of secreted IL-8 proteins, for all single-cell experiments. The fit to the theoretical distribution is shown as the continuous curve. Even for one cell there can be deviations from the bell-shaped theoretical functional form in the higher tail of the histogram due to autocrine signaling.

B.3.2. Theoretical approach

The essence of our approach is to regard the system, a single-cell (or a small colony), as not being in an equilibrium state because it is under the action of constraints. When the constraints are present the system is in that state of equilibrium that is possible under the constraints. This allows us to derive a quantitative version of the principle of Le Chatelier. Thereby we can quantitatively predict the response of the system to a (small) perturbation. Early on mathematical biologists expressed caution about the application of the Le Chatelier's principle to biological systems[25]. It is possible to directly use the measured experimental results to validate our point of view. The qualitative reasoning is straightforward and so we give it here. It is valid to apply the principle of Le Chatelier when the system is in a stable equilibrium. When is the system in a stable equilibrium? – when, under a small perturbation, it returns to its equilibrium state. Here we simply state that if the observed fluctuations in protein copy number are about a stable state then we can apply the principle of Le Chatelier. The stability of the state is decided by the experimental measurements. Both the notion of stability and the response to perturbations, as quantified in the principle of Le Chatelier, require that the departure from equilibrium be small. Neither textbook equilibrium thermodynamics applied to a macroscopic system nor the

extended theory used here to describe one or a few cells implies that under a 'large' perturbation it should be possible to displace a cell to a new stable state that is distinct from its unperturbed state. For a single-cell or small cell colony, the experiments reveal that cell-cell perturbations are indeed small. For larger cell colonies the statistics are not secure enough to make a clear-cut statement. We have, however, numerical indications that the unperturbed state of the single-cell is possibly unstable in the presence of many other cells.

B.3.3. Theory of fluctuations

We begin by considering a compartment containing a single-cell secreting different proteins. For different compartments the experiment shows a possibly different number of secreted proteins of a given type. We denote the experimentally measured copy number of protein *i* in a given microchamber by N_i. We impose the constraints that the distribution for each protein is characterized by the mean number of its molecules. Then the distribution, $P(N_i)$ of copy number fluctuations of a protein *i* that is of maximal physical entropy (= the distribution at physical equilibrium subject to constraints), is derived in Supplement, Eq. S2. It is a bell-shaped function of N_i with a single maximum.

In seeking the maximum of the entropy we require that the energy is conserved. This constraint is imposed by the method discussed in Supplement. This method introduces parameters into the distribution. *b* is determined by the constraint of conservation of energy and, as usual, is related to the temperature *T* as $\beta = 1/kT$ where *k* is Boltzmann's constant. The μ_i's are analogs of the chemical potentials as introduced in the thermodynamics of systems of more than one component. Here, however, we are dealing with many replicas of a single-cell isolated within a microchamber. Even though we deal with just a single-cell, the μ_i's will be shown in Eq. 1 below to also play the role of potentials. This means, for example, that the mean copy number $\bar{N}_i$ of protein *i* increases when its potential μ_i is increased. The mean number, $\bar{N}_i = \sum_i N_i P(N_i)$, is the average computed over the distribution. In operational terms this is an average computed over the different microchamber assays of protein *i*. We take it that the copy number distribution is normalized meaning that $\sum_i P(N_i) = 1$.

We next discuss the effect of perturbations on the distribution for a single-cell in the compartment. The regime of small perturbations is one in which the distribution, although perhaps distorted from a simple bell-shaped curve, still exhibits only a single maximum. The signature of large perturbations is that secondary maxima appear. When these become dominant a new state of the cell is prevailing.

To theoretically characterize the response of the cellular secretion to a perturbation we compute first the change in the distribution for the special case in which a perturbation changes the potential of protein *i* from μ_i to $\mu_i+\delta\mu_i$, where $\delta\mu_i$ is a small increment. We show (Eq. A2 in 3.6.3) that, to first-order in the change of the potential, the distribution changes by $\delta P\left(N_i\right)=\beta\left(\bar{N}_i-N_i\right)P\left(N_i\right)\delta\mu_i$. The result for δP has two immediate implications. One is that a perturbation will distort the shape of the distribution of the copy numbers of a given protein. Specifically, the change is proportional to the unperturbed distribution but its magnitude is weighted by the factor $\left(\bar{N}_i-N_i\right)$ so as to favor higher values of protein numbers. Thus, it is the high-end tail of the distribution that is most strongly influenced by the perturbation (see **Fig. B.6**., for example).

The other immediate implication of the change in the distribution is that the mean values will change. Specifically the updated mean value of the copy number of protein *i* when we change from μ_i to $\mu_i+\delta\mu_i$ is $\bar{N}_i+\delta\bar{N}_i=\sum_i N_i\left[P\left(N_i\right)+\delta P\left(N_i\right)\right]$. A technical point is that because the distribution needs to be normalized we must have $\sum_i\delta P\left(N_i\right)=0$. Using the result above that the change $\delta P\left(N_i\right)$ in the distribution is proportional to the unperturbed distribution and the normalization we arrive at the explicit result for the change in the mean copy number under a small disturbance.

$$\delta\bar{N}_i=\sum_i N_i\delta P\left(N_i\right)=\beta\delta\mu_i\sum_i N_i\left(\bar{N}_i-N_i\right)P\left(N_i\right)=\beta\delta\mu_i\overline{\left(\bar{N}_i-N_i\right)^2} \qquad (1)$$

This equality states that because the variance is positive, a change in the mean copy number of protein *i* when its own potential is changed from μ_i to $\mu_i+\delta\mu_i$ is always in the same direction (positive or negative) as $\delta\mu_i$ itself. It is in this sense that we refer to μ_i as the potential of protein *i*.

The key point that carries into the general case, is that, to linear order in the perturbation, the change in the mean number of proteins due to a perturbation can be computed as an average over the unperturbed distribution of copy numbers. The change in the mean is the variance of the distribution of fluctuations. Therefore, the lesser are the fluctuations (i.e., the narrower is the histogram), the more resilient to change is the distribution. As an example, IL-8 (**Fig. B.6.**) will be shown to be a very strongly coupled protein. IL-8 also has a particularly large variance as compared to the other proteins. Therefore there is some perturbation via autocrine signaling as seen in the hump in the higher tail of the histogram.

B.3.4. A quantitative Le Chatelier equation

With good measurement statistics one can examine the histogram for a joint distribution of two proteins and verify that pairs of proteins are correlated. Therefore the mean value (and other averages) of a protein *i* will change when protein *j* is perturbed. In the linear regime the result (see B.6.4.) is

$$\delta \bar{N}_i = \beta \sum_j \left[\overline{\left(\bar{N}_i - N_i \right) \left(\bar{N}_j - N_j \right)} \right] \delta \mu_j \qquad (2)$$

where the covariance is computed over the unperturbed distribution. Eq. 2 is valid in the linear regime of small perturbations, and indicates that the contributions of different perturbations add up. The covariance matrix $\boldsymbol{\Sigma}$, whose elements are $\boldsymbol{\Sigma}_{ij} = \overline{\left(N_j - \bar{N}_j \right) \left(N_i - \bar{N}_i \right)}$, is what is called in matrix algebra a positive matrix[26]. The implications of positivity are explored in B.6.5.

We prove in the B.6.4 that Eq. 2 is a quantitative statement of the principle of Le Chatelier in the meaning that a response to a perturbation changes the system in the direction of restoring a stable equilibrium. This is the analog of the observation that when we add energy (i.e., heat the system) the temperature goes up (rather than down). By equilibrium we mean a state of maximal entropy subject to the current value of all the constraints operating on the system. A system can therefore be maintained at equilibrium by imposing constraints such as keeping a gas under higher pressure at a fraction of the available volume of a cylinder. When these constraints are changed the system can move to a new equilibrium.

The covariance matrix is used in statistics as input in such methods of data analysis as principal component analysis[27,28]. We emphasize that for us the covariance matrix is derived by physical considerations leading to Eq. 2. We can thereby state that $\mathbf{\Sigma}_{ij}$ is quantitatively the change in the number of copies of protein *i* when protein *j* is perturbed. Note that while the covariance is a positive matrix, individual off-diagonal elements can be negative signifying inhibition. The covariance matrix in digital form is provided in **Table B.6.**

Table B.6. Digital representation of the covariance matrix for 1 cell measurements

COV	IL-2	MCP-1	IL-6	GMCSF	MIF	IFN-γ	VEGF	IL-1β	IL-10	IL-8	MMP9	TNF-α
IL-2	1.18E+06	-27830	7966.7	1.34E+05	2.30E+08	4.10E+06	85756	1.27E+06	1.60E+05	-1.06E+08	1.50E+07	2.31E+07
MCP-1	-27830	6.34E+09	-1.83E+05	-1.14E+06	-9.54E+09	-9.51E+07	6.10E+05	-3.31E+07	-2.52E+06	-8.51E+09	4.21E+09	-7.34E+08
IL-6	7966.7	-1.83E+05	9050.5	11507	1.56E+07	5.89E+05	734.25	4.20E+05	24714	-81623	-7.38E+05	1.04E+06
GMCSF	1.34E+05	-1.14E+06	11507	3.39E+05	3.75E+08	3.97E+06	53462	5.71E+06	2.07E+05	1.05E+07	-1.66E+07	1.75E+06
MIF	2.30E+08	-9.54E+09	1.56E+07	3.75E+08	3.12E+12	1.48E+10	-4.32E+08	1.19E+10	3.35E+08	-4.33E+11	-7.53E+10	-5.22E+10
IFN-γ	4.10E+06	-9.51E+07	5.89E+05	3.97E+06	1.48E+10	3.09E+08	-2.28E+05	1.40E+08	5.83E+06	-1.70E+09	-5.01E+08	-1.00E+08
VEGF	85756	6.10E+05	734.25	53462	-4.32E+08	-2.28E+05	2.48E+06	-2.65E+06	1.04E+05	9.34E+07	2.92E+07	2.59E+07
IL-1β	1.27E+06	-3.31E+07	4.20E+05	5.71E+06	1.19E+10	1.40E+08	-2.65E+06	4.78E+08	4.46E+06	1.86E+09	-4.08E+08	3.16E+08
IL-10	1.60E+05	-2.52E+06	24714	2.07E+05	3.35E+08	5.83E+06	1.04E+05	4.46E+06	7.39E+05	2.20E+08	-5.64E+06	2.92E+07
IL-8	-1.06E+08	-8.51E+09	-81623	1.05E+07	-4.33E+11	-1.70E+09	9.34E+07	1.86E+09	2.20E+08	2.73E+12	7.05E+09	3.56E+10
MMP9	1.50E+07	4.21E+09	-7.38E+05	-1.66E+07	-7.53E+10	-5.01E+08	2.92E+07	-4.08E+08	-5.64E+06	7.05E+09	3.70E+10	5.25E+09
TNF-α	2.31E+07	-7.34E+08	1.04E+06	1.75E+06	-5.22E+10	-1.00E+08	2.59E+07	3.16E+08	2.92E+07	3.56E+10	5.25E+09	5.26E+10

To summarize, the result for the distribution of protein copy numbers for the strongly interacting protein IL-8 (**Fig. B.6.**) has just one maximum. The noticeable deviations in the tail of the distribution are likely due to autocrine signaling, because the correlation of IL-8 with itself is only comparable in magnitude to the correlation of MIF with itself. Those two correlations are larger than any other variance or covariance. As discussed below, IL-8 is also strongly correlated with other proteins. For $n \geq 3$ cells in the microchamber, there is numerical evidence for a second maximum in the distribution of IL-8 fluctuations. For other proteins, six or more cells per chamber are required before a second maximum is resolved.

We can draw two conclusions from the fit of **Fig. B.6.**, between observed fluctuations and the theoretical result. First, the experimental distribution has but one maximum, and so the state is stable. Second, the theory accounts for the shape of the experimental distribution. This implies that we have correctly identified the important constraints on the system. Therefore we have Eq. 1 for the change of the distribution and hence Eq. 2 as the quantitative statement of the Le Chatelier's theorem. If there are additional constraints one can still derive a quantitative Le Chatelier's theorem but there will be additional terms beyond those shown explicitly in Eq. 2. We reiterate that Eq. 2 is the covariance computed from the experiments for an unperturbed cell. In our work below we use Eq. 2 to predict the effect of perturbation.

B.4. Results and Discussion

B.4.1. Computing the covariance matrix

The single-cell data (the heat map of Fig. **B.5.**) can be regarded as a rectangular matrix **X** where each row is a separate measurement and each column contains the copy number of a particular protein. For our convenience we mean center each column. When the number of measurements (= number of rows of **X**) is not small (and is ≥ than the number of columns) the covariance matrix can be immediately computed as $\mathbf{\Sigma}_{ij} = \sum_{k=1}^{K} X_{ki} X_{kj} \big/ K$ where k runs over all measurements, k =1,2,..,K. By construction of the matrix **X**, the matrix element X_{ki} is the number recorded in the k'th measurement for protein i minus the mean number $\bar{N}_i$ for that protein. We divide $\mathbf{X}^T\mathbf{X}$ by the number, K, of measurements so that the covariance is the mean value. The covariance is a product of the measured numbers, so the coefficient of variation of the covariance is, for small variations, twice the coefficient of variation of the measurements. An upper estimate, see **Table B.5.** and **Fig. B.6.**, is 14% when the covariance is computed from the fluorescence intensities. The conversion from the fluorescence intensity to the number of molecules does not change the coefficient of variation when we are in the linear regime of the calibration curve, see **Fig. B.2..** However at very low or high intensities the calibration curve is non-linear, so that small changes in fluorescence intensity are amplified to larger differences in the number of molecules, and thus large values of the variance. Out of K = 129 single-cell

experiments, we therefore eliminated four outliers. These corresponded to one instance each for which the fluorescence levels of TNF-α, IL-1β, MIF or IL-6 were very high. We thus used $K = 125$ values to compute the covariance matrix. The elimination of these four outliers brings the error of reading the number of molecules to be more comparable to the error in reading the fluorescence intensity.

B.4.2. The network

We analyze the covariance matrix in two stages. The first stage yields a quick (but correct and reliable) 'global' summary of the network, meaning which protein is coupled with which other proteins. There is finer structure, discussed below, that is not resolved in this first stage. To obtain the global network we begin by noting that the covariance matrix is symmetrical so that protein *i* is correlated with protein *j* just as much as protein *j* is correlated with protein *i*, $\mathbf{\Sigma}_{ij} = \mathbf{\Sigma}_{ji}$. This means that although both positive and inhibitory couplings can be extracted from the network, the direction of those coupling (i.e. protein *i* inhibits protein *j*, rather than vice-versa) is not resolved. The results for the overall network are shown in **Fig. B.7.** Panel A is the raw data for plotting the network and panel B is the network itself. The protein most strongly coupled to all others is MIF, and it is primarily anti-correlated with the other proteins. Next in strength of coupling is IL-8. Note that the symmetry between any two proteins is limited; proteins 1 and 2 may be coupled to each other, but protein 1 may be coupled to protein 3, while proteins 2 and 3 are uncorrelated. Mathematically this is possible because the total coupling strength of protein *i*, sum of $\mathbf{\Sigma}_{ij}$ over all *j*, can be quite different from the total coupling strength of protein *j* that is given as the sum of $\mathbf{\Sigma}_{ji}$ over all possible proteins *i*.

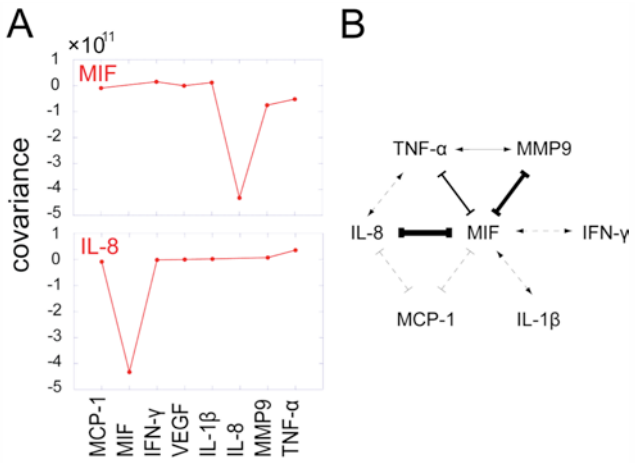

Fig. B.7. The summary network derived from the information theory treatment of the data. (A) It is these interdependencies, as revealed by the columns of the covariance matrix that provide the prediction of the connectivity in the network (part B). Shown are the columns for the two most connected proteins, MIF and IL-8. The entries are the covariances of the indicated protein with the other proteins listed in the abscissa. Self-correlations are not shown**.** (B) The protein correlation network hypothesis. The thickness of an arrow is an indication of correlation strength. Arrows indicate a positive correlation; bars indicate inhibition.

The covariance matrix shows the quantitative extent to which the fluctuations in any two proteins *i* and *j* are covarying. As discussed, about 14% of the value is due to noise. In the network we want to compare the relative importance of the covariance of proteins *i* and *j* to the covariance of proteins *l* and *m*. We take it that the covariance of proteins *l* and *m* should not be regarded as comparable to the covariance of *i* and *j* when the measured covariance of *l* and *m* is below the uncertainty due to noise of the covariance of *i* and *j*. We construct a graphical global summary of the interaction network by retaining only those proteins that are covarying with one or more other proteins above the noise level of the highest covarying pair of proteins. Below we discuss the components of the covariance matrix. Thereby we will have a measure of uncertainty for the entire matrix. It turns out that the criterion we use above is consistent with this measure.

The largest covariance, 4×10^{11} is between MIF and IL-8. This sets a boundary of 6×10^{10} on the covariances of pairs that we show as connected in the network. The large and positive magnitude of the covariance of MIF and IL-8 is shown as a double headed arrow. The arrow is double headed to denote the joint activation of one by the other. In the diagram,

inhibition is indicated, as usual, by a bar at the end of the connector. The dashed line correlations of MIF with IFN-g is of magnitude 2×10^{10}, and so may be corrupted by noise. The dashed line correlations between MIF and both MCP-1 and IL-1b are even weaker (about 10^{10}). The more refined analysis presented in Fig. 6 shows, however, that these two correlations are likely real and above the noise level.

Macrophages are an important source of IL-8 and MIF[29-31], and IL-8 is secreted by the macrophages without LPS stimulation, while MIF is secreted upon LPS stimulation (**Fig. B.8.A**). Our derived network model indicates the MIF is inhibited by IL-8, and MIF, in turn, inhibits 3 other proteins, including TNF-a, while it promotes the production of IL-1b. These predictions are consistent with the time-dependent measurements of secreted proteins (**Fig B.8.B**). From those measurements, we find that the levels of three proteins (MIF, TNF-a, and IL-1b) that are secreted upon LPS stimulation, exhibit fluctuations over time. The MIF and TNF-a temporal fluctuations are anti-correlated, consistent with the network hypothesis. A detailed elucidation of the underlying mechanism for these dynamics will require additional experiments. However, it is encouraging that a network hypothesis derived from single-time-point, single-cell data does provide consistent insight into the dynamical responses of the macrophages to stimulation.

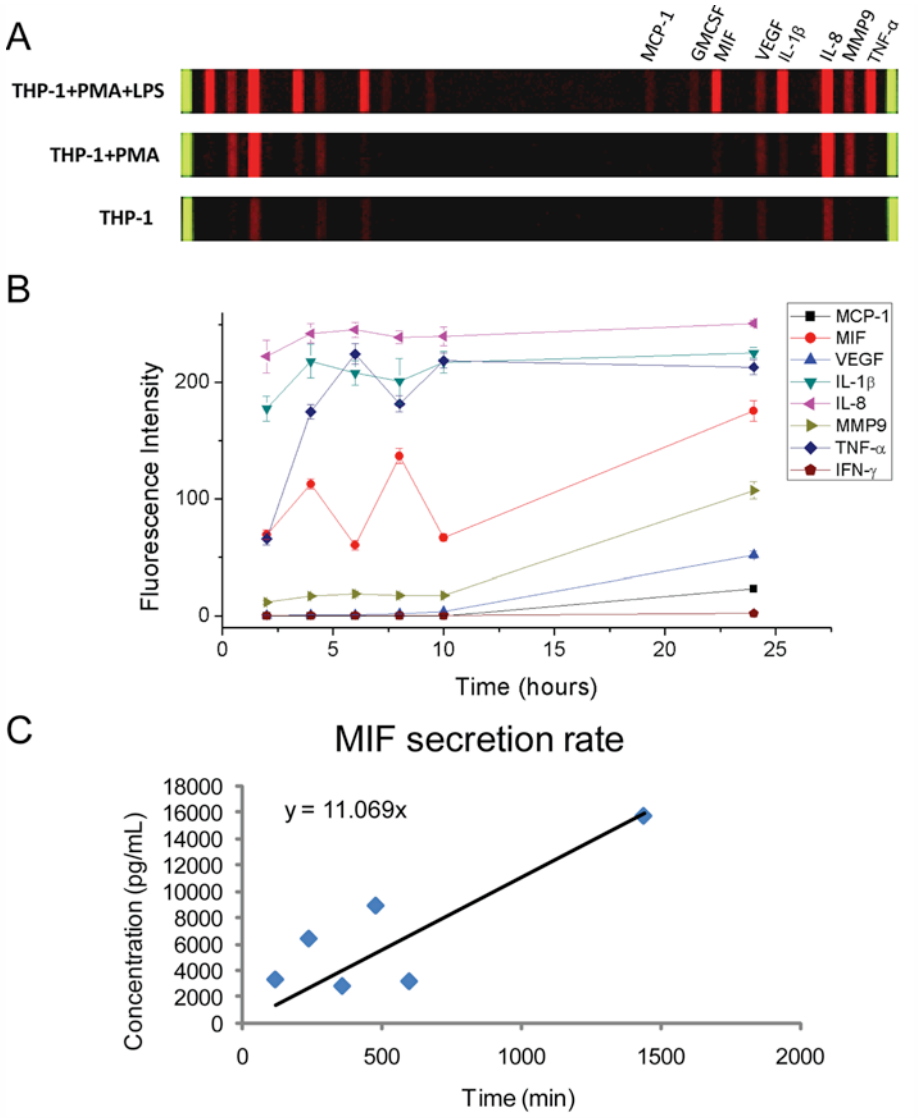

Fig. B.8. PMA and LPS activation and kinetics of protein secretion from activated macrophage cells. (A) Bulk secretion profiles from THP-1 cells under different conditions. PMA treatment induces THP-1 cells to macrophages and LPS treatment emulates innate immune responses against Gram-negative bacteria (B) Quantitation of bulk secretion intensities for the eight selected proteins over 24 hours. The samples were collected at 2, 4, 6, 8, 10, and 24 hours after incubation of PMA/LPS treated cells. The cell density was 0.3×10^6 cells/mL, which is a comparable density to a single-cell in a chamber of SCBC device. Note that the secretion levels of TNF-α and MIF are oscillatory and anti-correlated. (C) MIF secretion rate based on the assumption of linear time dependence from (B). The secretion rate from the bulk experiment is about 11 pg/mL per min which is about two-fold higher than the single-cell secretion data from the SCBC device (4.84 pg/mL per min).

B.4.3. The composite networks

In the second stage in our analysis of the covariance matrix we aim to show a more resolved structure and thereby note features that are glossed over in the global network of **Fig. B.7.B**. We will show that there are several independent networks operating together to globally represent **Fig. B.7.B.** The detailed analysis also provides a more robust error estimate. To resolve independent inherent structures within the covariance matrix we consider what is known in matrix algebra as the spectral representation (See B.6.6. and B.6.7 for more details). Technically this is a ranking of the eigenvectors as also carried out in principal component analysis. We suggest, however, that for our system specifically this ranking allows an examination of tiers in the cell-cell signaling. The tiers are independent, meaning that they govern independent fluctuations. The proteins that are members of a given tier respond collectively to a perturbation.

The spectral theorem[26] allows us to rank the contributions according to the decreasing magnitude of the eigenvalues. At the bottom are the smallest eigenvalues and these are attributed to experimental noise rather than to real biological information. For the single-cell in the compartment we find, as expected for the linear regime, that the dominant eigenvectors are each localized around a particular protein. As shown in **Fig. B.9.**, the two largest are localized on MIF and IL-8. The leading eigenvalue = tier 1, is only about 30% bigger than the second one, m =2. The third eigenvalues (not shown) is smaller by almost two orders of magnitude. **Fig. B.10.** is a plot on a logarithmic scale of all non-zero eigenvalues. There are only two eigenvectors that, judging by the value of their corresponding eigenvalues, are definitely above the noise.

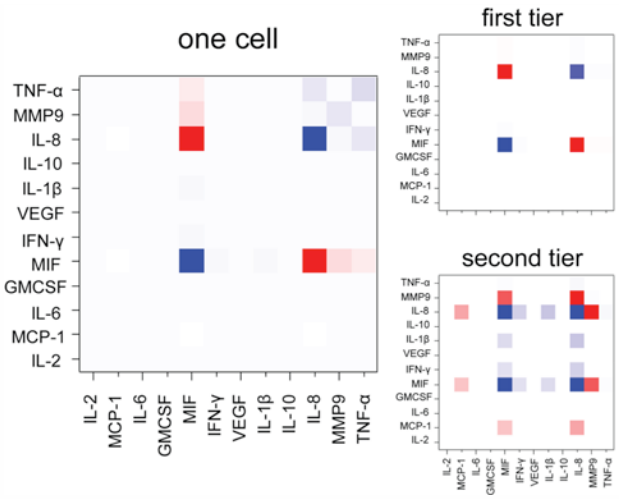

Fig. B.9. Protein-protein interactions via the quantitative Le Chatelier's theorem. Shown is the covariance matrix as a heat map for the single-cell, n=1 data (left) and the resolution of the matrix into the two most important tiers (right). Note the strong correlation of MIF and of IL-8 with the other proteins. Red implies inhibition and blue implies activation. The range is [-4e+11, 4e+11] for the covariance matrix shown in the left panel. This range is chosen to attenuate the high reading of the self-correlations in the covariance matrix. This heat map also provides a graphic representation of the protein interaction network. The ranges shown on the right-hand side are, respectively, top [-1.5e12, 1.5e12] and bottom [-2.9e10, 2.9e10].

In drawing **Fig. B.8.B** we could not state definitely that the correlations of MIF with IFN-g, MCP-1 and IL-1b, are above the noise level. The more refined spectral analysis shows that all these correlations are clearly evident in the second tier (**Fig. B.9.**) and so are secure. The **Fig. B.9.** results are the fluctuations measured for one cell experiments. See **Fig. B.11.** for similar results but for n =3 cells per microchamber.

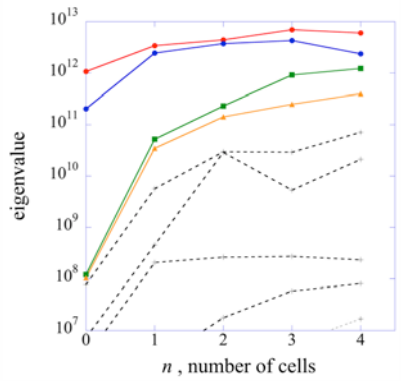

Fig. B.10. **The dependence of the dominant eigenvalues of the covariance matrix on the number of cells in the sample**. The result for n = 0, the background, is included to show the influence of the noise. The dashed lines, the fifth and higher eigenvalues are more corrupted by noise.

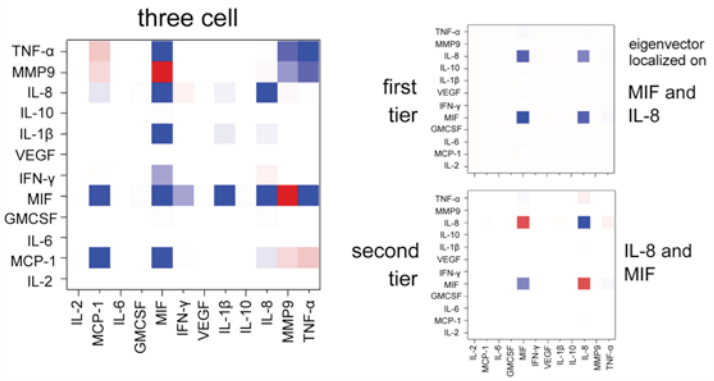

Fig. B.11. Heat map of the covariance matrix (left) and of the contributions to the first two tiers of the network (right) for measurements on chambers containing 3 cells. Similar to the single-cell case (**Fig. B.9.**), the entries in the tiers are scaled by the size of the eigenvalues. See the spectral representation of the covariance matrix, Eq. S11. The plot at left is the covariance matrix computed from the observed fluctuations in the 3-cell data. The color code is -8e+10 (red) to 0 (white) to +8e+10 (blue). The range is fixed so as to attenuate the effect of the self-terms in the covariance matrix. For tier 1 and tier 2, the ranges are [-4.3e-12, 4.3e+12] and [-7e+10,7e+10], respectively. Note that when the numbers of cells per chamber increases, anti-correlations can get washed out.

B.4.4. The number-based network

The network presented in **Fig. B.8.** and **Fig. B.9**. is based upon experimental measurements in which raw fluorescence intensities are converted into numbers of

molecules. We do this conversion because it is the numbers of molecules that are secreted by the cells, or to which the cells respond, that ultimately reflects the true biology. However, this conversion seemingly introduces an additional source of noise, especially when the measured fluorescence intensity is away from the linear regime of the calibration curves. However, this conversion yields an accurate reflection of the true measurements, and the accruing benefit is worthwhile. Specifically, the number of secreted proteins is independent of the very complicated experimental response function that depends upon the fluorescence detection methods, the various capture and detection antibodies used, and the fluorescence vs. concentration profiles that characterize calibration assays. We are thus able to apply the fundamental theory to quantitative molecular measurements, and so the resultant network is a more secure representation of the true cell biology, even if the accompanying experimental uncertainties are large relative to what would be estimated from pure fluorescence measurements.

B.4.5. Antibody perturbations

We performed an inter-cellular signaling perturbation study by adding neutralizing antibodies to eliminate specific secreted cytokines. For these experiments, 4 groups of microchambers within each SCBC chip were operated independently. Three neutralizing antibodies (anti-VEGF, anti-IL-8, and anti-TNF-a) were added to the cells, with one antibody per microchamber group. A control experiment was performed without any neutralizing antibody. As shown in **Fig. B.12.**, the removal of IL-8 markedly increased the production MIF, slightly increased IL-1b and slightly decreased TNF-a. The results are in agreement with the network hypothesis, **Fig. B.7.B.**

Using the theorem of Le Chatelier we quantitatively predict the effect of the antibody perturbations using Eq. 2. Here, the input for the prediction is the covariance matrix for the unperturbed cells. To compute the predicted mean number of protein *i* after an antibody for protein *j* is applied we need to know the change in chemical potential of protein *j*. We take it that an antibody for a protein lowers its chemical potential. We determine the magnitude of that reduction by requiring that the decrease in the copy number of the directly perturbed protein is reproduced. Additional details are provided in 3.6.9. The quality of the prediction in the perturbation experiments of IL-8 and VEGF is excellent, as shown in **Fig. B.12.** The

prediction of the results for the perturbation by anti-TNF-a is not in accord, likely because the change in the mean copy number of the proteins is smaller by about an order of magnitude, and so is close to the noise level.

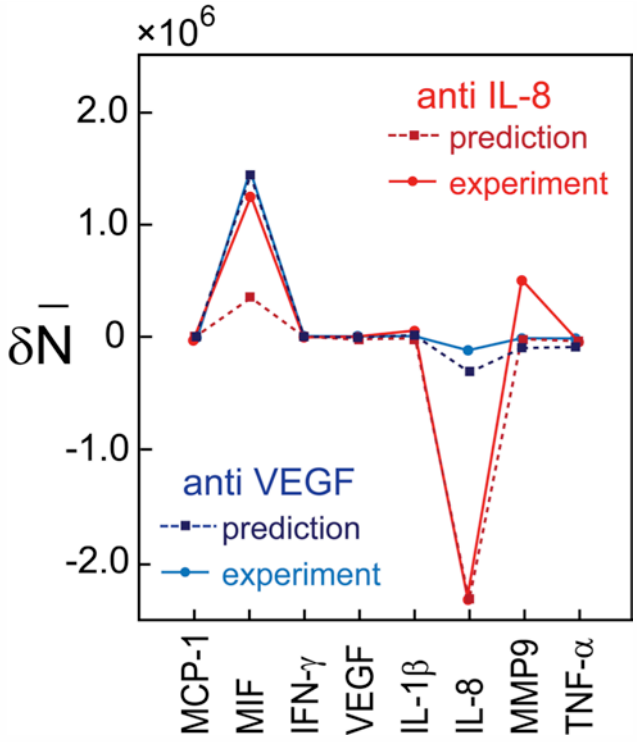

Fig. B.12. Perturbation of protein networks using neutralizing antibodies. The measured change in the mean number of eight proteins is compared against the predicted change, as computed from the fluctuations observed in the unperturbed single-cell data.

B.5. Conclusions

The multiplexed measurements of secreted proteins by single-cells and defined, few cell colonies provide a unique opportunity to capture the fluctuations of individual cells. An information theoretic, maximal entropy analysis can be applied to reproduce the observed fluctuations in the levels of the different assayed proteins. The theoretical analysis can also account for why for some proteins exhibit broad fluctuations, while others exhibit narrow fluctuations. The experimental approach permits observations of the covariance in the fluctuations of different proteins, and how those fluctuations evolve as a single-cell is

perturbed by the presence of 1,2,3, etc., other cells. Again, with the information theory, these covariances can be analyzed to extract hypotheses about the network of interacting proteins. Measuring the role of antibodies for specific proteins provides a test of that network hypothesis, and demonstrates that the theory is able to quantitatively *predict* the results of the molecular perturbation experiments using only data obtained for the unperturbed cells. This demonstration of the Le Chatelier's principle, appears to be general, and we are currently exploring how it can be applied towards understanding the role of other perturbations (such as hypoxia, genetic modifications, etc.). The long-term goal is to extend this approach toward understanding the various protein-signaling networks that operate within complex microenvironments, such as tumors.

B.6. Supplement: Details in Theoretical Methods

B.6.1. Introduction to theoretical supplementary methods

We show how to characterize protein-protein interactions. Specifically we show (*i*) that the different tiers of a signaling network can be quantitatively determined from the measured fluctuations in the concentrations of signaling proteins and (*ii*) that the measured fluctuations in the concentrations of signaling proteins for the unperturbed cell can be used to predict the effect of introducing perturbations such as neutralizing antibodies. The approach is developed from an information theoretic perspective and it is related to the specification of the direction of change when a system responds to a perturbation, known as the principle of Le Chatelier. The corresponding result here is that we predict the sequence of tiers in the network, see **Fig. B.7.** of the article. In addition we specify which signaling proteins are at a given tier of the network and their mutual influence including inhibition, see **Fig. B.9.** of the article. Experimental measurements of the fluctuation of concentrations in samples with nanoliter volume containing n cells, $n = 0,1,2,\ldots$, see Fig. S8 below, are used to validate the signaling protein network. Finally we use the protein-protein interaction as determined for the unperturbed cell to quantitatively predict, **Fig. B.12.** of the article, the effect of perturbations.

The approach we propose provides an analog and an extension of the statement that heat is transferred from a warmer to a colder body. We can understand this statement as a

statement about the direction of a process between two equilibrium states, meaning that it is a static principle. We can also think of it as a statement about the dynamics, meaning that it specifies the rate of change. We will here develop the formalism for the static interpretation. The explicit introduction of time is possible and we have the required formalism at hand but it requires a more elaborate theoretical foundation and so will be given elsewhere.

B.6.2. The ensemble: basis for making predictions

The system we consider is many independent replicas of a compartment containing a single-cell in a nutrient solution at thermal equilibrium. Because the system is not large, different replicas of it can differ in the number, N_i, of secreted proteins of kind *i*. We seek to represent these fluctuations by taking the different replicas as different samples from an ensemble of single-cell compartments where the mean number $\bar{N}_i$ of proteins of kind *i* over the ensemble is given. Another given quantity is the energy, (and volume that we do not indicate explicitly). We now seek the most probable distribution of protein numbers in different compartments. The solution is well known because if many compartments are measured then the required distribution is the one whose entropy is maximal. In textbooks of statistical mechanics this search for the most probable distribution is sometime called the Boltzmann approach. It is possible to show[32] that this approach does not require the system to be macroscopic in size. It is sufficient if we measure enough replicas so that the distribution of proteins does not significantly change as we add more measurements. If each replica is macroscopic the fluctuations will be small and rare. Repeated measurements will give the same results. If each replica is small we can observe the fluctuations, which is the experiment described in the main text.

The key point is that even if the fluctuations are not small it is possible to make predictions. We discuss three types of predictions in the paper, with more details given in this section of Supplement. We predict the distribution of fluctuations, we predict the tiers in the network and, in particular and as shown in **Fig. B.12.**, we predict the response of a system to a perturbation. For these first and last predictions, we compare directly with

experimental results. We emphasize that the prediction is made strictly independently of the experiment to which it is compared.

The probability of a system in a particular composition can be shown to be given by

$$P(N_1, N_2, ..) = \exp\left\{\beta\left(\sum_i \mu_i N_i - E\right)\right\}/\Xi \qquad \text{(S1)}$$

This straightforward result is perhaps misleading in its simplicity. It is most directly derived by the method of Lagrange undetermined multipliers. The numerical value of these multipliers is determined at the final stage by imposing the condition that the distribution (Eq. S1) reproduces the given values of the means. There are as many multipliers as conditions.

β is the Lagrange multiplier that is determined by the mean value of the energy and, as usual, is related to the temperature T as $\beta = 1/kT$ where k is Boltzmann's constant. The μ_i's are the chemical potentials as introduced in the thermodynamics of systems of more than one component[24,33]. The Lagrange multipliers that correspond to the given (mean) number of species i are known as the Planck potentials and denoted as α_i. It is often more convenient to work with μ_i, $\alpha_i = \beta\mu_i$. If our system were macroscopic in size we would call μ_i 'the chemical potential of protein i'. For convenience we retain the designation 'potential' because, as we shall show, μ_i retains essential properties of the chemical potential even when fluctuations are finite. Ξ is a function of all the Lagrange multipliers and its role is to insure that the sum of the probability over all possible compositions yields one.

There are at least two points where important details are not revealed by the notation used in Eq. S1. Both are relevant in what follows. First is the condition that the numerical values of the chemical potentials are determined by the given mean numbers, the $\bar{N}_i$'s, of the proteins. Strictly speaking, we should write the chemical potentials as functions of the $\bar{N}_i$'s. The other point arises when we want to treat the actual numbers N_i's of the different proteins as continuous variables. This is needed, for example, to compute averages, normalize the distribution (Eq. S1), etc. The integration for each protein

is over $dN/N!$ where $N!$, the factorial of N, arises to account for the Gibb's paradox. Therefore, as a function of the continuous variable N the distribution for, say, one protein is

$$P(N) \propto \left(Q^N/N!\right)\exp(-\beta\mu N) \tag{S2}$$

Here Q is the factor that arises by summing over all the internal states of the protein that are occupied at the temperature T. This result is used in the main text to fit the observed distribution for a single protein (**Fig. B.6.).**

B.6.3. Fluctuations describe the response to small perturbations.

We show that by measuring the fluctuations in the unperturbed system we can predict how the system responds to small perturbations[33]. Proof: Say that we make a small change in the value of the chemical potential μ_i from its current equilibrium value to some new value $\mu_i + \delta\mu_i$. We do so isothermally. This change in m_i potentially changes the equilibrium mean concentration of all species from $\bar{N}_j$ to $\bar{N}_j + \delta\bar{N}_j$, for all j. To compute the change in concentrations we need to consider the change in the ensemble as represented by Eq. S1. In the algebraic developments in Eq. S4 below we make use of the definition of the mean concentration

$$\bar{N}_j = \sum N_j P(N_1, N_2, ..) \tag{S3}$$

The summation in Eq. S3 is over all the possible compositions, each weighted by its probability $P(N_1, N_2, ..)$ computed as the distribution of maximal entropy. The same meaning for the summation is used also in Eq. S4 below. We denote this averaging by an over bar. From Eq. S1, the variation of the distribution that occurs when a particular chemical potential is changed by a small amount is $\delta P(N_1, N_2, ..) = \beta\,\delta\mu_i\, N_i P(N_1, N_2, ..)$. Note that it is in using this lowest term in the Taylor series that we assume that the change is small. It follows that on the average the proteins respond to the change as:

$$\begin{aligned}\delta \bar{N}_j &= \sum N_j \, \delta P(N_1, N_2, ..) \\ &= \sum \left(N_j - \bar{N}_j\right) \delta P(N_1, N_2, ..) \\ &= \beta \, \delta \, \mu_i \sum \left(N_j - \bar{N}_j\right) N_i P(N_1, N_2, ..) \\ &= \beta \, \delta \, \mu_i \sum \left(N_j - \bar{N}_j\right)\left(N_i - \bar{N}_i\right) P(N_1, N_2, ..) \\ &= \beta \, \delta \, \mu_i \overline{\left(N_j - \bar{N}_j\right)\left(N_i - \bar{N}_i\right)}\end{aligned} \tag{S4}$$

Note that the conservation of normalization implies that the average change in the probability must be zero, $0 = \sum \delta P(N_1, N_2, ..)$ and we have used this result in the derivation above. In the last line in Eq. S4 we have avoided writing the summation over all compositions by the use of the over bar to designate an average over the probability $P(N_1, N_2, ..)$, which is the notation introduced in Eq. S3.

Taylor theorem states that, in the leading order, the change of a function is the sum of the changes. Therefore the expression for an isothermal variation in all the chemical potentials leads to a change of the distribution of the form:

$$\delta P(N_1, N_2, ..) = \beta \sum_i N_i P(N_1, N_2, ..) \delta \mu_i \tag{S5}$$

The summation in Eq. S5 is an ordinary sum over the finite number *S* of signaling proteins, $i = 1, 2, .., S$. Then we have the general equation of change that is an extended form of Eq. S4 valid for all possible small isothermal changes in the chemical potentials

$$\delta \bar{N}_j = \beta \sum_i \overline{\left(N_j - \bar{N}_j\right)\left(N_i - \bar{N}_i\right)} \, \delta \mu_i \tag{S6}$$

B.6.4. The principle of Le Chatelier

The principle in its simplistic statement claims that the system responds to a perturbation in a direction that restores equilibrium. For example, when the temperature of a heat bath is increased the mean energy of an immersed system goes up so that the distribution remains canonical. The proof for our case starts from Eq. S3. When the chemical potential of protein *i* is changed, for an ensemble at maximal entropy the mean value of protein *j* changes by

$$\frac{\partial \bar{N}_j}{\partial \mu_i} = \sum N_j \frac{\partial P(N_1, N_2, ..)}{\partial \mu_i} \tag{S7}$$

where, as emphasized in Eq. S3, the distribution $P(N_1, N_2, ..)$ is not arbitrary but is the one of maximal entropy as exhibited in Eq. S1. Eq. S4 is recovered when the derivative in Eq. S7 is evaluated. The reader may feel that this is a triviality but it is not without meaning. What we have proven is that computing a small change in the distribution $P(N_1, N_2, ..)$ when a particular chemical potential is changed from the value μ_i to a new value $\mu_i + \delta\mu_i$ is the same as computing the derivative of the distribution $P(N_1, N_2, ..)$ at the point where the value of the chemical potential is μ_i. Then the change in the distribution is $\left(\partial P(N_1, N_2, ..)/\partial \mu_i\right)\delta\mu_i$. Of course, this is what differential calculus is about. Yet the result is not pure mathematics. It shows that the new distribution is a distribution of maximal entropy of the functional form Eq. S1 as otherwise the result will not hold. It says that a small change in the chemical potential μ_i, and no other change, leads to a new distribution which is also one of maximal entropy.

Typically we do not see the theorem of Le Chatelier stated as in Eq. S6. This is because of the practical point that the number fluctuations are typically not easy to observe in a macroscopic system. Here however we deal with secretion of proteins by a single-cell and, as shown in the main text and particularly in the histogram in **Fig. 3.6.**, the distribution is clearly observed and the covariance can be computed from the experimental data as long as that the number of replicas is not small.

B.6.5. The equation for the direction of change

The (symmetric) square matrix $\overline{\left(N_j - \bar{N}_j\right)\left(N_i - \bar{N}_i\right)}$ is the covariance matrix of the (equilibrium) fluctuations in the (equilibrium) concentrations, the $\bar{N}_j$'s. It is an equilibrium average because, as explicitly shown in Eq. S4, it is an expectation over the equilibrium distribution as given in Eq. S3. The covariance matrix has the dimensions of *S* by *S* where *S* is the number of signaling molecules that take part. In practice we have to

compromise on this definition meaning that *S* is the number of signaling molecules that can be detected. If an important protein is not detected then the network that we infer will be incomplete.

A covariance matrix can be shown to be a non-negative matrix, also called semipositive definite, meaning that its eigenvalues are zero or positive. If the concentrations of the signaling proteins can in principle be varied independently, which is definitely not necessarily the case, then the covariance matrix $\overline{\left(N_j - \bar{N}_j\right)\left(N_i - \bar{N}_i\right)}$ is a positive matrix with positive eigenvalues. We will discuss below why it will often be the case that for reasons of both principle and practice (e.g., experimental noise) there will be eigenvalues that are effectively zero. In that case, technically, the covariance matrix is positive semidefinite[34].

Eq. S6 specifies how the concentration of the *j*'th signaling molecule varies when the *i*'th chemical potential is changed. In general the correlation coefficient $\overline{\left(N_j - \bar{N}_j\right)\left(N_i - \bar{N}_i\right)}$ between the signaling molecules *i* and *j* can be either positive or negative. Therefore, in general the change $\delta \bar{N}_j / \delta \mu_i$ is not necessarily of the same direction for all proteins *j*. This obvious result will be important for us below. Using the observation that the covariance matrix is semipositive definite, it is however possible to determine the direction of change by first diagonalizing the covariance matrix. This means that we can determine *S* distinct linear combinations of signaling molecules, where (*a*) each such set of molecules changes in a given direction and (*b*) we can order the different sets in terms of the extent of their response such that the first set is the most changing, the second set changes to a lesser extent, etc. In the time-dependent formalism, not presented here, we can outright say that the first set is the fastest changing and therefore it is the first to change. Then there follow changes in the second set, etc. It is clearly our intention to identify each set of signaling molecules as the set of molecules in a given tier in the network.

B.6.6. Tiers of the network are eigenvectors of the correlation matrix

Our next purpose is to define the tiers of the network. The set of proteins that participate in the *m*'th tier is determined as follows. Let $\mathbf{S}_m$ designate the *m*'th eigenvector of the covariance matrix where the eigenvectors are listed in order of decreasing magnitude of the corresponding eigenvalue. The largest eigenvalue is *m* =1. Each eigenvector $\mathbf{S}_m$ is a (column) vector of *S* components and it is determined by the matrix equation

$$\mathbf{\Sigma}\,\mathbf{S}_m = \sigma_m^2\,\mathbf{S}_m \quad , \; m = 1, 2, . \tag{S8}$$

where $\mathbf{\Sigma}$ is the *S* by *S* symmetric covariance matrix whose elements are $\mathbf{\Sigma}_{ij} = \overline{\left(N_j - \bar{N}_j\right)\left(N_i - \bar{N}_i\right)}$ and we explicitly indicated that the eigenvalues are positive or zero but not negative (which defines a positive semidefinite matrix). The eigenvectors of the symmetric covariance matrix are orthogonal to one another and can be chosen to be normalized

$$\mathbf{S}_{m'}^T \cdot \mathbf{S}_m = \begin{cases} 0, & m' \neq m \\ 1, & m' = m \end{cases} \tag{S9}$$

Here the superscript *T* designates the transpose so that $\mathbf{S}_{m'}^T$, is a row vector and Eq. S9 is the scalar product.

For each value of the number of cells, *n*, in the compartment the eigenvalues are arranged in the order of decreasing magnitude the largest eigenvalue being labeled as *m* =1 and the smallest as *m* =12. See **Fig. B.10.** for the dependence of the largest eigenvalues vs. cell number.

B.6.7. The spectral representation of the covariance matrix

Fig. B.9. shows the covariance matrix computed for experiments with one cell in the compartment. Also shown in **Fig. B.9**. is the resolution of the covariance matrix into tiers defined as follows. From each eigenvector $\mathbf{S}_m$ we can define an *S* by *S* symmetric matrix $\mathbf{P}_m$ as follows

$$\mathbf{P}_m = \mathbf{S}_m \cdot \mathbf{S}_m^T \tag{S10}$$

The spectral theorem (10) is the result that the covariance matrix $\mathbf{\Sigma}$ can be resolved into tiers as

$$\mathbf{\Sigma} = \sum_m \sigma_m^2 \mathbf{P}_m \tag{S11}$$

The eigenvalues σ_m^2 are arranged in a decreasing order so that each subsequent tier makes a smaller contribution. The very dominant contribution is from m =1 The leading eigenvalue = tier 1, is only about 30% bigger than the second one, m =2. The third eigenvalue is smaller by almost two orders of magnitude. **Fig. B.10.** is a plot on a logarithmic scale of all non-zero eigenvalues. There are only two eigenvectors that, judging by the value of their corresponding eigenvalues are definitely above the noise. The dominant (m=1) and the m = 2 eigenvectors for 1 cell measurements are shown in **Fig. B.9.** and for three cells in **Fig. B.11.**

B.6.8. The role of the number of cells in the sample

It was possible to make repeated measurements of the protein concentrations for different values of the number of cells in the sample. In this section we argue that the direction of increasing n can be semi-quantitatively regarded as a direction of increasing time. Therefore by examining how the eigenvectors of the covariance matrix change with n we have an independent determination of the direction of the *dynamic* response of the system.

Fig. B.10. shows are the largest eigenvalues for n = 0, 1, 2, 3 and 4 cells. To interpret **Fig. B.10.** within the point of view as used in this paper we argue as follows. A single-cell secretes a number of different signaling proteins and therefore even the data measured for a single-cell can show the role of protein-protein interactions. If two cells are in the sample these interactions increase in importance. If we think of n as a measure of concentrations of proteins then $\bar{N} \propto n$ but to compute the covariance we need to divide by the number of protein molecules. So for both paracrine and endocrine signaling we expect

the covariance to increase with *n*. When *n* becomes high there may be three or more cells interacting and the simple considerations break down.

B.6.9. Antibody perturbations

Fig. B.12. shows a quantitative comparison of the measured results as compared to the purely theoretical prediction when neutralizing antibodies for specific proteins are added. We emphasize that it is a prediction because the results shown are based on using Eq. S4 that we repeat here:

$$\delta \bar{N}_j = \beta \overline{\left(N_j - \bar{N}_j\right)\left(N_i - \bar{N}_i\right)} \delta \mu_i = \beta \boldsymbol{\Sigma}_{ji} \delta \mu_i$$

The addition of a neutralizing antibody for protein *i* means that $\delta \mu_i$ is negative. We emphasize that the experimental results shown in **Fig. B.12.** are for single-cells in the compartment. This means, see **Fig. B.10.** that the largest eigenvalue, $\sigma^2_{m=1}$, of the covariance matrix is large indeed. Then, from Eq. S11, the contribution from the first tier dominates. It is the two proteins in this tier that are shown in the panel. There are bigger discrepancies between theory and experiment for tiers 2 or 3 for which the experimental signal is weak.

B.7. References

1. Lin, W.-W. & Karin, M. A cytokine-mediated link between innate immunity, inflammation, and cancer. *J Clin Invest* **117,** 1175–1183 (2007).
2. Gnecchi, M. *et al.* Paracrine action accounts for marked protection of ischemic heart by Akt-modified mesenchymal stem cells. *Nature Publishing Group* **11,** 367–368 (2005).
3. Croci, D. O. *et al.* Dynamic cross-talk between tumor and immune cells in orchestrating the immunosuppressive network at the tumor microenvironment. *Cancer Immunol. Immunother.* **56,** 1687–1700 (2007).
4. Seruga, B., Zhang, H., Bernstein, L. J. & Tannock, I. F. Cytokines and their relationship to the symptoms and outcome of cancer. *Nat Rev Cancer* **8,** 887–899

(2008).

5. Polyak, K. & Weinberg, R. A. Transitions between epithelial and mesenchymal states: acquisition of malignant and stem cell traits. *Nat Rev Cancer* **9,** 265–273 (2009).
6. Ariztia, E. V., Lee, C. J., Gogoi, R. & Fishman, D. A. The tumor microenvironment: key to early detection. *Crit Rev Clin Lab Sci* **43,** 393–425 (2006).
7. Sachs, K., Perez, O., Pe'er, D., Lauffenburger, D. A. & Nolan, G. P. CaUSAl protein-signaling networks derived from multiparameter single-cell data. *Science* **308,** 523–529 (2005).
8. Nomura, L., Maino, V. C. & Maecker, H. T. Standardization and optimization of multiparameter intracellular cytokine staining. *Cytometry A* **73,** 984–991 (2008).
9. Lamoreaux, L., Roederer, M. & Koup, R. Intracellular cytokine optimization and standard operating procedure. *Nat Protoc* **1,** 1507–1516 (2006).
10. Cox, J. H., Ferrari, G. & Janetzki, S. Measurement of cytokine release at the single-cell level using the ELISPOT assay. *Methods* **38,** 274–282 (2006).
11. Song, M. & Phelps, D. S. Comparison of SP-A and LPS effects on the THP-1 monocytic cell line. *Am. J. Physiol. Lung Cell Mol. Physiol.* **279,** L110–7 (2000).
12. Fan, R. *et al.* Integrated barcode chips for rapid, multiplexed analysis of proteins in microliter quantities of blood. *Nat Biotechnol* **26,** 1373–1378 (2008).
13. Shin, Y. S. *et al.* Chemistries for patterning robust DNA microbarcodes enable multiplex assays of cytoplasm proteins from single cancer cells. *Chemphyschem* **11,** 3063–3069 (2010).
14. Quake, S. R. & Scherer, A. From micro- to nanofabrication with soft materials. *Science* **290,** 1536–1540 (2000).
15. Millet, L. J., Stewart, M. E., Sweedler, J. V., Nuzzo, R. G. & Gillette, M. U. Microfluidic devices for culturing primary mammalian neurons at low densities. *Lab Chip* **7,** 987–994 (2007).
16. Lee, J. N., Park, C. & Whitesides, G. M. Solvent compatibility of poly(dimethylsiloxane)-based microfluidic devices. *Anal. Chem.* **75,** 6544–6554 (2003).

17. Altschuler, S. J. & Wu, L. F. Cellular heterogeneity: do differences make a difference? *Cell* **141,** 559–563 (2010).
18. Wang, J. *et al.* A self-powered, one-step chip for rapid, quantitative and multiplexed detection of proteins from pinpricks of whole blood. *Lab Chip* **10,** 3157–3162 (2010).
19. Findlay, J. W. A. & Dillard, R. F. Appropriate calibration curve fitting in ligand binding assays. *AAPS J* **9,** E260–7 (2007).
20. Levine, R. D. Information theory approach to molecular reaction dynamics. *Annu Rev Phys Chem* **29,** 59–92 (1978).
21. Levine, R. D. Information Theoretical Approach to Inversion Problems. *Journal of Physics a-Mathematical and General* **13,** 91–108 (1980).
22. Remacle, F. & Levine, R. D. The Elimination of Redundant Constraints in Surprisal Analysis of Unimolecular Dissociation and Other Endothermic Processes. *J Phys Chem A* **113,** 4658–4664 (2009).
23. Jaynes, E. T. Probability theory: The logic of science. *Cambridge University Press* (2004).
24. Mayer, J. E. & Mayer, M. G. *Statistical mechanics*. (Wiley, 1977).
25. Lotka, A. J. Note on moving equilibra. *P Natl Acad Sci USA* **7,** 168–172 (1921).
26. Bellman, R. *Introduction to Matrix Analysis*. (McGraw-Hill, 1970).
27. Wall, M. E., Rechtsteiner, A. & Rocha, L. M. in *Approach to Microarray Data Analysis* 91–109 (Kluwer Academic Publishers, 2003). doi:10.1007/0-306-47815-3_5
28. Jolliffe, I. T. *Principal Component Analysis*. (Springer Verlag, 2002).
29. Roger, T., David, J., Glauser, M. P. & Calandra, T. MIF regulates innate immune responses through modulation of Toll-like receptor 4. *Nature* **414,** 920–924 (2001).
30. Calandra, T., Bernhagen, J., MITCHELL, R. A. & Bucala, R. Macrophage Is an Important and Previously Unrecognized Source of Macrophage-Migration Inhibitory Factor. *J Exp Med* **179,** 1895–1902 (1994).
31. Murphy, K. P., Travers, P., Walport, M. & Janeway, C. *Janeway's immunobiology*. (Garland Pub, 2008).

32. Levine, R. D. How large is ‘large’ for a thermodynamic-like behavior. *Physica E* **9,** 591–599 (2001).
33. Callen, L. *Thermodynamics and an Introduction to Thermostatistics*. (Wiley, 1985).
34. Alhassid, Y. & Levine, R. D. Experimental and Inherent Uncertainties in the Information Theoretic Approach. *Chemical Physics Letters* **73,** 16–20 (1980).